Journal of Materials Chemistry A

ROYAL SOCIETY OF CHEMISTRY

PAPER

View Article Online
View Journal

Cite this: DOI: 10.1039/d5ta03041b

Redox-active metal–organic framework as an anode-active material for rechargeable aqueous manganese dioxide batteries with very high-rate capabilities

Ryota Akai, [a] Hitoshi Kasai[a] and Kouki Oka *[abc]

Rechargeable aqueous manganese-based batteries are attracting considerable attention because they consist of Earth-abundant elements, are environmentally friendly, and exhibit high theoretical capacity. To avoid deteriorating battery performance owing to dendrite formation on the zinc anode surface, organic-manganese dioxide batteries using redox-active organic materials as the anode-active material feature dendrite-free and highly durable charge storage. However, organic anode-active materials usually suffer from poor counterion diffusion, and their low conductivity prevents electron conduction to the interior of the materials, rechargeable aqueous organic-manganese dioxide batteries exhibiting a discharge capacity close to the theoretical capacity and high coulombic efficiency have not been previously achieved. In the current work, we fabricated a novel rechargeable aqueous metal–organic framework (MOF)-manganese dioxide battery with a redox-active MOF as the anode-active material, which provided pores for efficient ion diffusion and a small particle size to promote electron conduction throughout the material. The developed battery exhibited a discharge capacity close to theoretical capacity (>99% of the theoretical capacity), high coulombic efficiency (99%), and high-rate capabilities, while maintaining high cyclability.

Received 17th April 2025
Accepted 11th November 2025

DOI: 10.1039/d5ta03041b

rsc.li/materials-a

Introduction

The recent widespread use of vehicles and portable electronics has driven the requirement for energy storage devices, with lithium-ion batteries (LIBs) and lead–acid batteries (LABs) dominating the global market.[1,2] LIBs exhibit high energy and power densities and are mainly used in mobile devices.[3,4] LABs are mainly used in vehicles owing to their low cost and facile maintenance.[5,6] However, LIBs contain scarce elements (*e.g.*, cobalt and nickel) and flammable electrolytes.[3,4] LABs use lead as the electrode-active material, which exhibits low energy and power density, and its toxicity conflicts with current environmental regulations.[5,6] To achieve large-scale energy-storage systems suitable for a sustainable society, new technologies based on abundant resources and harmless aqueous-based electrolytes are required.[7–9]

In recent years, rechargeable aqueous manganese-based batteries have attracted considerable interest due to their high theoretical capacity and use of Earth-abundant and low-toxicity materials and aqueous electrolytes.[9,10] Most of these batteries store charge *via* a two-electron MnO_2/Mn^{2+} mechanism, and other valence states of manganese (Mn^0, Mn^{2+}, Mn^{3+}, Mn^{4+}, and Mn^{7+}) could be applied to innovative rechargeable aqueous manganese-based batteries.[11] State-of-the-art rechargeable aqueous zinc–manganese dioxide batteries using zinc featuring a negative electrode potential (−0.76 V *vs.* SHE) exhibited high voltage (approximately 1.5 V); however, dendrite formation on the surface of the zinc anode during charge/discharge cycling degraded cyclability over time.[12] Therefore, to improve battery performance, it is necessary to develop dendrite-free anode-active materials and exhibit high cyclability.

Unlike metal and inorganic electrode-active materials, organic materials consist of Earth-abundant elements, their functionality is highly tunable by controlling the molecular design,[13–18] and they do not form dendrites. Rechargeable aqueous organic-manganese dioxide batteries have been fabricated using organic materials such as organic molecules,[19–29] polymers,[30–35] and covalent-organic frameworks[36,37] as anode-active materials. These batteries exhibited high cyclability, and their voltage and discharge capacity were modulated by controlling the molecular design.[19–37] However, organic materials tended to aggregate preventing efficient counterion diffusion,[38] and their low conductivity prevented electron conduction to the interior of the materials.[39–41] Therefore, rechargeable aqueous organic-manganese dioxide batteries exhibiting a discharge capacity close to the theoretical capacity

[a]*Institute of Multidisciplinary Research for Advanced Materials, Tohoku University, 2-1-1 Katahira, Aoba-ku, Sendai, Miyagi 980-8577, Japan. E-mail: oka@tohoku.ac.jp*
[b]*Carbon Recycling Energy Research Center, Ibaraki University, 4-12-1 Nakanarusawa, Hitachi, Ibaraki 316-8511, Japan*
[c]*Deuterium Science Research Unit, Center for the Promotion of Interdisciplinary Education and Research, Kyoto University, Yoshida, Sakyo-ku, Kyoto 606-8501, Japan*

and high coulombic efficiency have not been previously reported.

In the current work, we utilized metal–organic frameworks (MOFs) as anode-active materials, based on the hypothesis that their high crystallinity would enable efficient counterion diffusion and their small particle size would enhance electron conductivity throughout the material.[42–45] Among the numerous MOFs, we selected UiO-66 because it exhibited high stability in acidic aqueous solutions.[46,47] We prepared UiO-66-$(OH)_2$, which exhibited reversible charge storage capabilities in an acidic aqueous electrolyte in the presence of manganese ions. A novel rechargeable aqueous MOF-manganese dioxide battery with UiO-66-$(OH)_2$ as the anode-active material, MnO_2 as the cathode-active material, and 1 M $MnSO_4$ + 0.05 M H_2SO_4 aqueous electrolyte, respectively, was demonstrated. This battery demonstrated excellent performance, achieving a discharge capacity close to theoretical capacity (>99% of the theoretical capacity), very high coulombic efficiency (99%), and high-rate capability, while maintaining high cyclability.

Results and discussion

Characterization of UiO-66-$(OH)_2$

As illustrated in Fig. 1a, UiO-66-$(OH)_2$ was synthesized using a microwave method. In electrode-active materials with low conductivity, charge carriers are well-known to be conducted to a depth of up to 100 nm from the conductive surface.[48] Therefore, by reducing the microwave reaction time and concentration, as illustrated in the scanning electron microscopy (SEM) image in Fig. 1b, we prepared UiO-66-$(OH)_2$ of an average particle size of 70 ± 30 nm. As illustrated in Fig. 1c and d, the Brunauer–Emmett–Teller (BET) surface area and pore size of UiO-66-$(OH)_2$ were evaluated based on nitrogen gas adsorption/desorption isotherms measured at 77 K. The BET surface area was 578 $m^2\ g^{-1}$, and the pore-size distribution demonstrated peaks at 0.6 and 1.2 nm, which were considerably larger than the radius of the hydronium ion (0.10 nm).[32] The powder X-ray diffraction (PXRD) pattern for UiO-66-$(OH)_2$ in Fig. 1e indicated that it had the same crystal structure as simulated UiO-66 reported previously.[49] In addition, UiO-66-$(OH)_2$ maintained its crystallinity even after immersion in a 1 M $MnSO_4$ + 0.05 M H_2SO_4 aqueous solution for 24 h, indicating its high stability in the electrolyte. Thermogravimetric analysis (TGA) weight-loss curves for UiO-66-$(OH)_2$ were illustrated in Fig. 1f and S2. Three weight-loss steps were observed, corresponding to desorption of the adsorbed water, dehydration of the Zr clusters, and decomposition of 2,5-dihydroxyterephthalic acid (organic linker).[50–52] Analysis of these curves confirmed that the prepared UiO-66-$(OH)_2$ had 4.20 linkers per Zr cluster, whereas the theoretical number of linkers was 6 per Zr cluster. Therefore, the molecular weight and theoretical capacity were 1598.5 g mol^{-1} and 140.8 mAh g^{-1}, respectively. (The detailed

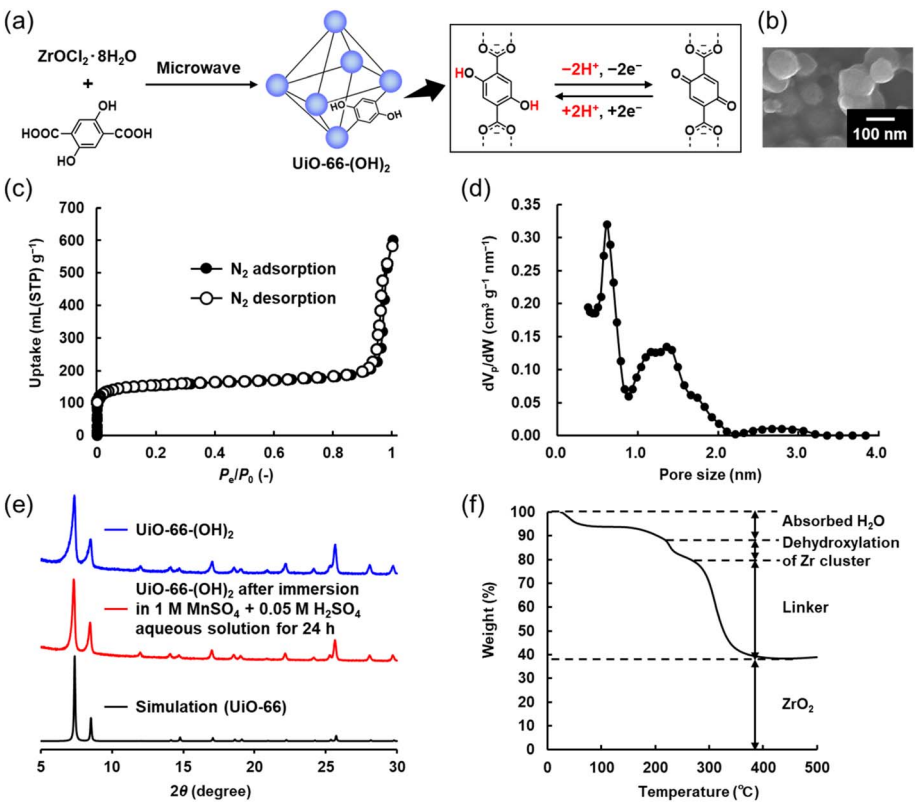

Fig. 1 (a) Synthesis process for UiO-66-$(OH)_2$. (b) SEM image of UiO-66-$(OH)_2$. (c) Nitrogen adsorption isotherms of UiO-66-$(OH)_2$ measured at 77 K. After measurement, UiO-66-$(OH)_2$ maintained its crystallinity (Fig. S1). (d) Pore-size distribution of UiO-66-$(OH)_2$. (e) PXRD patterns of simulation of UiO-66 (ref. 49) (black), as-synthesized UiO-66-$(OH)_2$ (blue), and UiO-66-$(OH)_2$ after immersion in 1 M $MnSO_4$ + 0.05 M H_2SO_4 aqueous solution for 24 h. (f) TGA weight-loss curve of UiO-66-$(OH)_2$ in air.

calculation method is described in Experimental sections S2.2 and S2.7).

Electrochemical properties of UiO-66-$(OH)_2$

The electrochemical properties of UiO-66-$(OH)_2$ in 1 M $MnSO_4$ + 0.05 M H_2SO_4 aqueous electrolyte were characterized. In order to avoid possible oxidation of Mn^{2+} ions by dissolved oxygen,[53–55] the following electrochemical measurements were performed under an argon atmosphere. Following the procedure described in Experimental section S2.3, we prepared UiO-66-$(OH)_2$/graphene mesosponge (GMS)[56,57] composite electrodes at a mass loading of UiO-66-$(OH)_2$ of approximately 0.5 mg. As illustrated in Fig. 2a UiO-66-$(OH)_2$/GMS composite electrode exhibited an irreversible oxidation peak at approximately +0.70 V *vs.* Ag/AgCl in the first cycle, corresponding to the extraction of protons hydrogen-bonded to carboxyl groups.[58] Once the electrode was oxidized, the redox peak at +0.11 V *vs.* Ag/AgCl was dominant compared to the irreversible oxidation peak at +0.70 V *vs.* Ag/AgCl, presumably because the reformation of the hydrogen bonds took a long time.[58] The molecular electrostatic potential (MESP) mapping by density functional theory (DFT)[26,59] revealed that oxygen atoms of the *p*-benzoquinone moiety exhibited significant negative MESP values (red), supporting their suitability for proton storage. The MESP mapping also showed relatively positive values (blue) of OH moieties of Zr–OH sites, indicating high affinity for proton uptake. The DFT calculations supported efficient proton insertion and extraction for fast charging and discharging of the UiO-66-$(OH)_2$/GMS composite electrode.[60] As illustrated in Fig. 2a and S4, a UiO-66-$(OH)_2$/GMS composite electrode exhibited redox peaks at $E_{1/2}$ = +0.11 V *vs.* Ag/AgCl in a 1 M $MnSO_4$ + 0.05 M H_2SO_4 aqueous electrolyte, $E_{1/2}$ = +0.15 V *vs.* Ag/AgCl in a 0.05 M H_2SO_4 aqueous electrolyte, and −0.12 V *vs.* Ag/AgCl in a 1 M $MnSO_4$ aqueous electrolyte, suggesting that the 1,4-dihydroxybenzene moiety in a 1 M $MnSO_4$ + 0.05 M H_2SO_4 aqueous electrolyte exhibited charge storage with two electrons and two protons.[9,24,61,62]

To evaluate the mobility of protons in the pore, the proton conductivity of UiO-66-$(OH)_2$ was measured by electrochemical impedance spectroscopy (EIS). The resulting Cole–Cole plot in Fig. 2b exhibited dielectric relaxation in the high-frequency region. Fitting this plot using an equivalent circuit[64] in Fig. S5 gave a proton conductivity of 2.49×10^{-6} S cm^{-1} at 95% relative humidity (RH) and 25 °C. As illustrated in Fig. S6, the direct current (DC) resistance measurements yielded a DC electrical conductivity of 2.72×10^{-9} S cm^{-1}. The value of 2.49×10^{-6} S cm^{-1} was much larger than 2.72×10^{-9} S cm^{-1}, supporting that 2.49×10^{-6} S cm^{-1} was the proton conductivity. The Arrhenius plot in Fig. S7 gave an activation energy (E_a) of 1.57 eV, which was larger than 0.4 eV, suggesting that proton conduction in UiO-66-$(OH)_2$ predominantly occurred *via* the vehicle mechanism.[65] Water-coordinated linker defects in UiO-

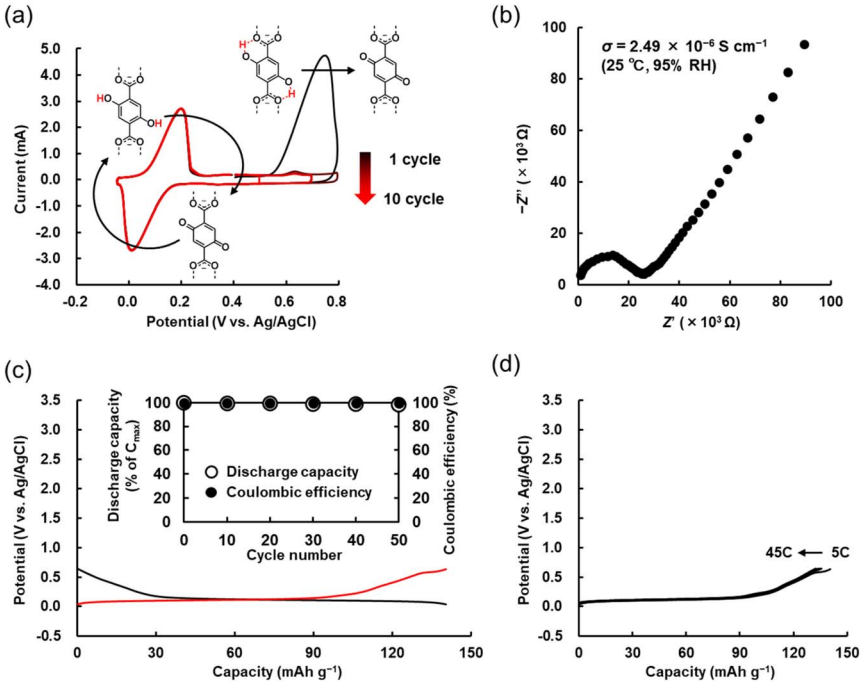

Fig. 2 (a) Cyclic voltammogram of a UiO-66-$(OH)_2$/GMS composite electrode in a 1 M $MnSO_4$ + 0.05 M H_2SO_4 aqueous electrolyte measured under an Ar atmosphere at a scan rate of 10 mV s^{-1}. (b) Cole–Cole impedance spectrum for a disk-shaped pellet of UiO-66-$(OH)_2$ measured at 95% RH and 25 °C. As shown in Fig. S6, we measured the impedance and the direct current resistance in the through-plane (through-thickness) direction of the pelletized sample, which had a diameter of 10 mm and a thickness of 0.45 mm. The flattened semicircles represented the bulk and grain boundary resistances.[63] The crystallinity was maintained even after impedance measurements (Fig. S4). (c) Charging (black)/discharging (red) profiles of the UiO-66-$(OH)_2$/GMS composite electrode at 5C. (Inset) Cycle test of the electrode at 20C. (d) Rate capabilities of the UiO-66-$(OH)_2$/GMS composite electrode at 5, 10, 20, 30, and 45C.

66 generated terminal Zr–OH_2 and Zr–OH sites.[49] These hydrated defects served as proton donors, and the coordinated and adsorbed water molecules enabled proton conduction predominantly, in which mobile protons diffused within the pore.[51] Therefore, although the theoretical capacity decreased depending on the number of linker defects, they provided continuous diffusion pathways of protons within the pore, which led to fast proton/charge transport of UiO-66-$(OH)_2$ (ref. 51) for high-rate capabilities of the UiO-66-$(OH)_2$/GMS composite electrode. The TGA data in Fig. 1f exhibited that UiO-66-$(OH)_2$ preferentially adsorbed water, and protons moved quickly in the pores based on the vehicle mechanism, suggesting that UiO-66-$(OH)_2$ should exhibit high-rate capabilities when used as an electrode-active material.

As illustrated in Fig. 2c, in a 1 M $MnSO_4$ + 0.05 M H_2SO_4 aqueous electrolyte, the UiO-66-$(OH)_2$/GMS composite electrode exhibited a plateau potential at +0.15 V *vs.* Ag/AgCl. The discharge capacity of the electrode was 140.5 mAh g^{-1}, which was close to the theoretical capacity (140.8 mAh g^{-1}) estimated from the molecular weight of UiO-66-$(OH)_2$. Based on small particle size (<100 mm) and high porosity (BET surface area: 578 m^2 g^{-1} and dominant pore size: 0.62 nm), ions in the electrolyte could efficiently enter the pores, and almost all organic linkers store protons and electrons. As shown in Fig. S10, in order to clarify the possible contribution of GMS and PVdF, a control experiment using a GMS/PVdF composite electrode was conducted under the same electrochemical conditions. The resulting discharge capacity of the GMS/PVdF composite electrode was less than 5% of that obtained for the UiO-66-$(OH)_2$/GMS composite electrode, indicating the contribution from GMS was negligible (which was also discussed in ref. 24). Therefore, as shown in Fig. 2a, the observed capacity was attributed predominantly to the UiO-66-$(OH)_2$. As illustrated in Fig. 2c inset, the UiO-66-$(OH)_2$/GMS composite electrode maintained more than 98% of the initial discharge capacity after 50 cycles. Inductively coupled plasma-mass spectrometry (ICP-MS) revealed that the amount of dissolved Zr detected in the electrolyte was less than 8 atom% of the total Zr initially present in the anode. This minor dissolution was most likely attributed to Zr–OH_2 and Zr–OH groups located at linker defect or edge sites, which have been reported to be labile in acidic aqueous solutions.[66–68] In contrast, the coordination bonds of Zr–OC were highly robust owing to their high bond energy of 766.1 kJ mol^{-1}.[69] In addition, the PXRD measurements and SEM images before and after cycle test exhibited no noticeable degradation (Fig. S11 and S12), as discussed in detail in the next batteries' section, and the discharge capacity decreased by only 2% after 50 cycles (Fig. 2c) and remained nearly unchanged thereafter. These results demonstrated that the organic linkers responsible for charge storage were retained and that UiO-66-$(OH)_2$ maintained its crystallinity in a 1 M $MnSO_4$ + 0.05 M H_2SO_4 aqueous solution, even in the presence of linker defects. As illustrated in Fig. 2d, even at 45C, a discharge capacity of the electrode was 132.5 mAh g^{-1} (94% of that at 5C close to the theoretical capacity) owing to the high proton conductivity in the pores of UiO-66-$(OH)_2$. As shown in Fig. S13, from the variation of peak potentials with scan rate using the Laviron method,[70] the apparent rate constants (k_0) for both oxidation and reduction were estimated to be 6.2×10^{-2} s^{-1}. The value of k_0 of the UiO-66-$(OH)_2$/GMS electrode was several times higher than that of previously reported redox-active organic materials.[30,71,72] As a result, the UiO-66-$(OH)_2$/GMS electrode would be expected to exhibit outstanding rate performance. As illustrated in Fig. S11 and S14, a MnO_2 (ε-phase[20,24,26]) electrode in 1 M $MnSO_4$ + 0.05 M H_2SO_4 aqueous electrolyte exhibited a redox reaction at +0.10 V *vs.* Ag/AgCl ($Mn^{2+} + 2H_2O \leftrightarrows MnO_2 + 4H^+ + 2e^-$).[9]

As described above, UiO-66-$(OH)_2$ achieved a discharge capacity close to the theoretical capacity and high coulomb efficiency (>99%) based on its high crystallinity facilitating counterion diffusion and on its small particle size controlled by the synthesis method, while maintaining high cyclability (>98% after 50 cycles).

Rechargeable aqueous MOF-manganese dioxide batteries

As shown in Fig. 3a and b, rechargeable aqueous MOF-manganese dioxide batteries were fabricated with a MnO_2 cathode, UiO-66-$(OH)_2$/GMS composite anode, and 1 M $MnSO_4$ + 0.05 M H_2SO_4 aqueous electrolyte. The MnO_2 electrode was prepared by electrodeposition[30] (see Experimental section S2.5 for details). As illustrated in the charging/discharging curves in Fig. 3c, the plateau voltage and coulombic efficiency of the battery were 0.84 V and >99%, respectively. As illustrated in Fig. 3c, since the discharge capacity was 140.1 mAh g^{-1} (close to the theoretical capacity of 140.8 mAh g^{-1} estimated from the molecular weight), almost all of the organic linkers participated in proton and electron storage. As shown in Fig. 3c inset, the battery exhibited high cyclability, maintaining 99% of the initial capacity after 50 cycles. As shown in Fig. S11 and S12, the PXRD measurements and SEM images demonstrated that UiO-66-$(OH)_2$ and MnO_2 retained their original crystalline structure and morphology even after 50 cycles, indicating their high structural and morphological stability. As shown in Fig. S15, a long-term cycle test of the rechargeable aqueous MOF-manganese dioxide battery was also performed. The battery retained 95% of its initial capacity even after 1000 cycles, demonstrating relatively high cyclability compared to other batteries listed in Table S2. In addition, the rate capabilities in Fig. 3d illustrated that, even at a very high-rate of 45C, the rechargeable aqueous MOF-manganese dioxide battery had a discharge capacity of 135.1 mAh g^{-1}, which was 96% of the theoretical capacity, presumably because UiO-66-$(OH)_2$ had high porosity and crystallinity for efficient counterion diffusion as described above. The battery delivered a maximum power density of 5327 W kg^{-1} at 45C, estimated based on the mass of the anode-active material (see Experimental section S2.7 for details). As shown in Fig. S16, a cycle test of the battery at different C-rates was also performed. At the highest rate of 45C, the discharge capacities remained unchanged during charge and discharge, confirming the high stability and reversibility of the battery under high-rate operation.

Fig. 3e, f and S17, along with Table S2, summarize the advantages of the rechargeable aqueous MOF-manganese dioxide battery compared to previously reported rechargeable aqueous organic-manganese dioxide batteries.[19–37] As illustrated in Fig. 3e and S9, our new battery design exhibited a discharge

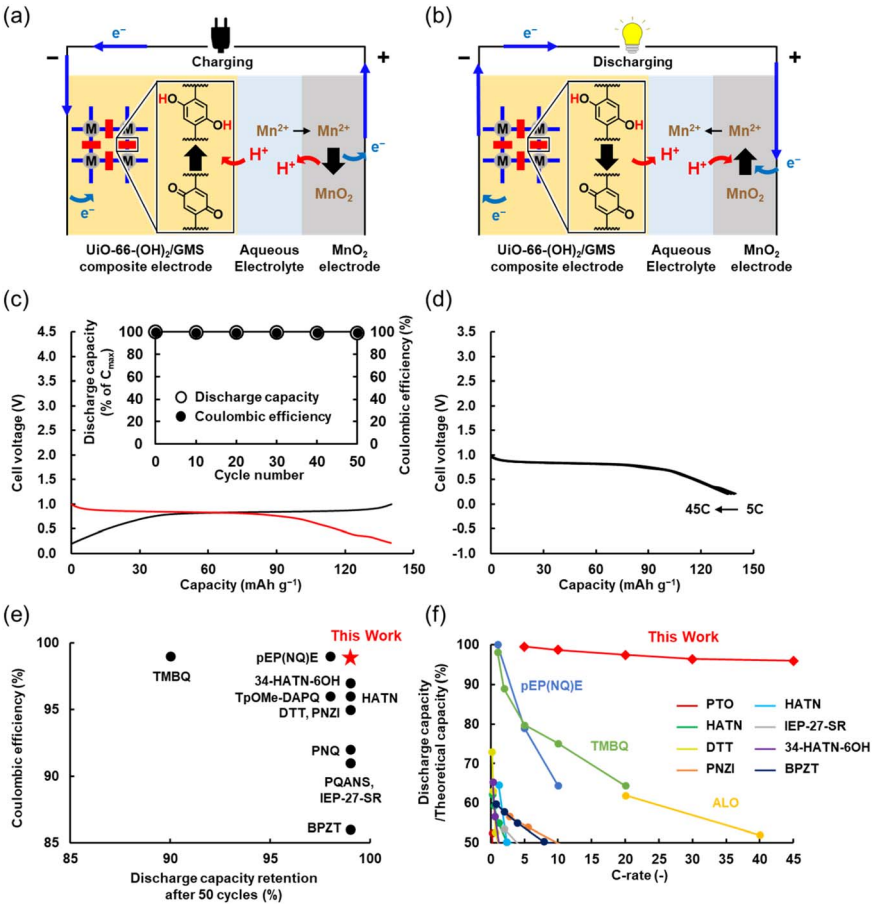

Fig. 3 Schematics of the rechargeable aqueous MOF-manganese dioxide battery during (a) charging and (b) discharging. (c) Charging (black)/discharging (red) profiles of the battery at 5C. (Inset) Cycle test of the battery at 20C. (d) Rate capability of the battery at 5, 10, 20, 30, and 45C. Comparison of (e) discharge capacity retention and coulombic efficiency and (f) discharge capacity/theoretical capacity for our battery compared with other recently developed batteries from the literature. The corresponding details are summarized in Table S2.

capacity close to theoretical capacity (>99% of the theoretical capacity) and high coulombic efficiency (99%) while maintaining high cyclability (99% of the initial capacity after 50 cycles). In addition, as shown in Fig. 3f, based on the high porosity and crystallinity for efficient counterion diffusion, the battery exhibited superior rate capabilities compared to the previously reported rechargeable aqueous organic-manganese dioxide batteries. Such rechargeable aqueous manganese dioxide batteries with high-rate capabilities are particularly advantageous for practical applications such as grid-scale stationary energy storage systems for load-levelling and buffering in renewable energy systems, where rapid charging/discharging responses are essential for stabilizing power fluctuations.[73,74] From the above, the rechargeable aqueous MOF-manganese dioxide battery in the current work achieved charge storage with almost the theoretical capacity and high coulombic efficiency for the first time, while maintaining high cyclability. In addition, toward the development of batteries exhibiting high power density, we demonstrated the advantages of MOFs with high porosity and crystallinity for efficient counterion diffusion. In our continuous work, we will address the cell design and cathode/anode balance optimization for practical battery configurations.

Conclusions

In the current work, we fabricated a novel rechargeable aqueous MOF-manganese dioxide battery with redox-active MOF as an anode-active material, which characterized pores for efficient counterion diffusion and a small particle size to promote electron conduction throughout the material, MnO_2 as a cathode-active material, and a 1 M $MnSO_4$ + 0.05 M H_2SO_4 aqueous solution as an electrolyte. The battery demonstrated superior performance compared to previously reported rechargeable aqueous organic-manganese dioxide batteries; a discharge capacity close to theoretical capacity (>99% of theoretical capacity), high coulombic efficiency (99%), and high cyclability (99% after 50 cycles). The rechargeable aqueous MOF-manganese battery in the current work achieved charge storage with almost the theoretical capacity and high coulombic efficiency for the first time, while maintaining high cyclability. In other words, the current work demonstrated the advantages of MOFs with high porosity and crystallinity for efficient counterion diffusion, toward the development of aqueous devices exhibiting high power density and cyclability. In our continuous work, we aim to improve the theoretical capacity and enhance the energy and power densities for practical high-rate batteries. We will develop redox-active MOFs incorporating

redox-active metals in their metal clusters while maintaining high stability in acidic aqueous solutions, guided by the hard and soft acids and bases (HSAB) principle, which strongly influences the acid stability of coordination bonds in MOFs.[47] In addition, to reduce or eliminate the use of conductive additives, we aim to further improve the intrinsic electronic conductivity of redox-active MOFs by developing acid-resistant electrically conductive MOFs.[75]

Author contributions

Ryota Akai: conceptualization, methodology, formal analysis, data curation, investigation, writing – original draft, funding acquisition, and resources. Hitoshi Kasai: writing – review & editing. Kouki Oka: conceptualization, methodology, formal analysis, data curation, project administration, validation, supervision, writing – original draft, writing – review & editing, funding acquisition, resources, and software.

Conflicts of interest

There are no conflicts to declare.

Data availability

The data supporting this article have been included as part of the supplementary information (SI). Supplementary information is available. See DOI: **https://doi.org/10.1039/d5ta03041b**.

Acknowledgements

This work was partially supported by Grants-in-Aids for Scientific Research (no. JP23K17945, JP23H03827, JP24K01552, JP24KJ1576, JP25K21722, JPJSBP120258801) from MEXT, Japan. This work was partially supported by the Environment Research and Technology Development Fund (JPMEERF20241RA4) of the Environmental Restoration and Conservation Agency provided by the Ministry of the Environment of Japan. K. O. also acknowledges the support from the Shorai Foundation for Science and Technology, TEPCO Memorial Foundation, Amano Industry Technology Laboratory, Sugiyama Houkoukai, The Yamada Science Foundation, Kenjiro Takayanagi Foundation, Kansai Research Foundation for Technology Promotion, Yashima Environment Technology Foundation, JACI Prize for Encouraging Young Researcher, Iketani Science and Technology Foundation, Foundation for Interaction in Science & Technology, and Kato Foundation for Promotion of Science (KS-3416). R. A. also acknowledges the support from the Hosokawa Powder Technology Foundation and the Mishima Kaiun Memorial Foundation.

References

1 A. Nekahi, A. K. Madikere Raghunatha Reddy, X. Li, S. Deng and K. Zaghib, *Electrochem. Energy Rev.*, 2024, **8**, 1.
2 S. Wolf and J. Olarte, in *Emerging Battery Technologies to Boost the Clean Energy Transition: Cost, Sustainability, and Performance Analysis*, ed. S. Passerini, L. Barelli, M. Baumann, J. Peters and M. Weil, Springer International Publishing, Cham, 2024, pp. 85–102, DOI: **10.1007/978-3-031-48359-2_6**.
3 N. Nasajpour-Esfahani, H. Garmestani, M. Bagheritabar, D. J. Jasim, D. Toghraie, S. Dadkhah and H. Firoozeh, *Renew. Sustain. Energy Rev.*, 2024, **203**, 114783.
4 J. M. Tarascon and M. Armand, *Nature*, 2001, **414**, 359–367.
5 G. J. May, A. Davidson and B. Monahov, *J. Energy Storage*, 2018, **15**, 145–157.
6 Y. Zhang, C.-G. Zhou, J. Yang, S.-C. Xue, H.-L. Gao, X.-H. Yan, Q.-Y. Huo, S.-W. Wang, Y. Cao, J. Yan, K.-Z. Gao and L.-X. Wang, *J. Power Sources*, 2022, **520**, 230800.
7 Z. Ju, Q. Zhao, D. Chao, Y. Hou, H. Pan, W. Sun, Z. Yuan, H. Li, T. Ma, D. Su and B. Jia, *Adv. Energy Mater.*, 2022, **12**, 2201074.
8 Y. Liang and Y. Yao, *Nat. Rev. Mater.*, 2023, **8**, 109–122.
9 M. Shi, P. Das, Z.-S. Wu, T.-G. Liu and X. Zhang, *Adv. Mater.*, 2023, **35**, 2302199.
10 H. Li, W. Zhang, K. Sun, J. Guo, K. Yuan, J. Fu, T. Zhang, X. Zhang, H. Long, Z. Zhang, Y. Lai and H. Sun, *Adv. Energy Mater.*, 2021, **11**, 2100867.
11 W. Chen, G. Li, A. Pei, Y. Li, L. Liao, H. Wang, J. Wan, Z. Liang, G. Chen, H. Zhang, J. Wang and Y. Cui, *Nat. Energy*, 2018, **3**, 428–435.
12 J. Luan, H. Yuan, J. Liu and C. Zhong, *Energy Storage Mater.*, 2024, **66**, 103206.
13 R. Akai, N. Tohnai and K. Oka, in *Batteries*, Jenny Stanford Publishing, 2024, pp. 155–216.
14 J. Kim, Y. Kim, J. Yoo, G. Kwon, Y. Ko and K. Kang, *Nat. Rev. Mater.*, 2023, **8**, 54–70.
15 X. Kong, S. Zhou, M. Strømme and C. Xu, *Carbon*, 2021, **171**, 248–256.
16 M. A. Navarra, J. Manzi, L. Lombardo, S. Panero and B. Scrosati, *ChemSusChem*, 2011, **4**, 125–130.
17 S. Wiratchan, T. Autthawong, W. Yodying, S. Surinwong, T. Konno, T. Sarakonsri and N. Semakul, *Chem. Eng. J.*, 2023, **466**, 143090.
18 T.-R. Kuo, L.-Y. Lin, S. Kubendhiran, Y.-C. Li, R.-J. Chung and S. Yougbaré, *J. Energy Storage*, 2022, **53**, 105085.
19 Y. Dai, X. Yan, J. Zhang, C. Wu, Q. Guo, J. Luo, M. Hu and J. Yang, *Electrochim. Acta*, 2023, **442**, 141870.
20 Z. Guo, J. Huang, X. Dong, Y. Xia, L. Yan, Z. Wang and Y. Wang, *Nat. Commun.*, 2020, **11**, 959.
21 Y. Ma, Y. Wei, W. Han, Y. Tong, A. Song, J. Zhang, H. Li, X. Li and J. Yang, *Angew. Chem., Int. Ed.*, 2023, **62**, e202314259.
22 T. Sun, H. Du, S. Zheng, J. Shi and Z. Tao, *Adv. Funct. Mater.*, 2021, **31**, 2010127.
23 S. Wu, H. Guo, Z. Su, C. Jia, X. Zhang, S. Wang, T. Zhao, Q. Meyer and C. Zhao, *Adv. Funct. Mater.*, 2024, **34**, 2315706.
24 X. Yang, Y. Ni, Y. Lu, Q. Zhang, J. Hou, G. Yang, X. Liu, W. Xie, Z. Yan, Q. Zhao and J. Chen, *Angew. Chem., Int. Ed.*, 2022, **61**, e202209642.
25 J. Yu, J. Li, Z. Y. Leong, D.-s. Li, J. Lu, Q. Wang and H. Y. Yang, *Mater. Today Energy*, 2021, **22**, 100872.
26 Y. Wang, C. Wang, W. Wang, Y. Zhang, Z. Guo, J. Huang, L. Yan, J. Ma and Y. Wang, *ACS Energy Lett.*, 2023, **8**, 1390–1396.
27 C. Wang, D. He, H. Wang, J. Guo, Z. Bao, Y. Feng, L. Hu, C. Zheng, M. Zhao, X. Wang and Y. Wang, *Adv. Sci.*, 2024, **11**, 2401314.

28 G. Zhao, X. Yan, Y. Dai, X. Wang, Z. Wang, B. Wang, R. Li, Y. Hao, H. Yu, H. Ma, H. Li, C. Wu, J. Liu, M. Hu and J. Yang, *Small*, 2024, **20**, 2406962.
29 M. Yang, Y. Hao, B. Wang, Y. Wang, L. Zheng, R. Li, H. Ma, X. Wang, X. Jing, H. Li, M. Li, Z. Wang, Y. Dai, G. Shan, M. Hu, J. Luo and J. Yang, *Natl. Sci. Rev.*, 2024, **11**, nwae045.
30 K. Oka, R. Löfgren, R. Emanuelsson, H. Nishide, K. Oyaizu, M. Strømme and M. Sjödin, *ChemElectroChem*, 2020, **7**, 3336–3340.
31 C. Strietzel, K. Oka, M. Strømme, R. Emanuelsson and M. Sjödin, *ACS Appl. Mater. Interfaces*, 2021, **13**, 5349–5356.
32 W. Han, M. Li, Y. Ma and J. Yang, *Electrochim. Acta*, 2022, **403**, 139550.
33 J. Yang, P. Shao, X. Zhao, Y. Liao and C. Yan, *J. Colloid Interface Sci.*, 2023, **650**, 1811–1820.
34 H. Wang, J. Yang, Y. Cui, J. He, J. Yang, L. Hu, M. Shi and C. Yan, *Chem. Eng. J.*, 2024, **499**, 156034.
35 R. Grieco, A. Fombona-Pascual, N. Patil, D. Alvan, M. Liras and R. Marcilla, *Batteries Supercaps*, 2025, **8**, e202400346.
36 T. Günther, D. Hedbom, M. Åhlén, H. Yoshino, H. Miyasaka, H. Kasai, K. Oka and R. Emanuelsson, *ChemPlusChem*, 2024, **89**, e202400184.
37 L. Cai, L. Lu, Y. Lan, Y. Zhang, J. Wang, Z. Lin, R. Li, F. Zhang, J. Yu, W. Lu, X. Bai and W. Wang, *Adv. Energy Mater.*, 2023, **13**, 2301631.
38 F. Ye, Q. Liu, H. Dong, K. Guan, Z. Chen, N. Ju and L. Hu, *Angew. Chem., Int. Ed.*, 2022, **61**, e202214244.
39 T. Sun, J. Xie, W. Guo, D.-S. Li and Q. Zhang, *Adv. Energy Mater.*, 2020, **10**, 1904199.
40 R. Akai, K. Oka, S. Dekura, H. Mori and N. Tohnai, *Bull. Chem. Soc. Jpn.*, 2022, **95**, 1178–1182.
41 R. Akai, K. Oka, S. Dekura, K. Yoshimi, H. Mori, R. Nishikubo, A. Saeki and N. Tohnai, *J. Phys. Chem. Lett.*, 2023, **14**, 3461–3467.
42 R. Akai, H. Kasai and K. Oka, *Nanoscale*, 2025, **17**, 9920–9925.
43 L. Jiao, J. Y. R. Seow, W. S. Skinner, Z. U. Wang and H.-L. Jiang, *Mater. Today*, 2019, **27**, 43–68.
44 H. Wang, Q.-L. Zhu, R. Zou and Q. Xu, *Chem*, 2017, **2**, 52–80.
45 Y. J. Kim, S. Y. Ko, S. Kim, K. M. Choi and W.-H. Ryu, *Small*, 2023, **19**, 2206561.
46 J. Winarta, B. Shan, S. M. McIntyre, L. Ye, C. Wang, J. Liu and B. Mu, *Cryst. Growth Des.*, 2020, **20**, 1347–1362.
47 C. Xiao, J. Tian, Q. Chen and M. Hong, *Chem. Sci.*, 2024, **15**, 1570–1610.
48 W. Choi, D. Harada, K. Oyaizu and H. Nishide, *J. Am. Chem. Soc.*, 2011, **133**, 19839–19843.
49 C. A. Trickett, K. J. Gagnon, S. Lee, F. Gándara, H.-B. Bürgi and O. M. Yaghi, *Angew. Chem., Int. Ed.*, 2015, **54**, 11162–11167.
50 L. Valenzano, B. Civalleri, S. Chavan, S. Bordiga, M. H. Nilsen, S. Jakobsen, K. P. Lillerud and C. Lamberti, *Chem. Mater.*, 2011, **23**, 1700–1718.
51 J. M. Taylor, S. Dekura, R. Ikeda and H. Kitagawa, *Chem. Mater.*, 2015, **27**, 2286–2289.
52 O. Haidar, T. Roques-Carmes, A. Gouda, N. Tabaja, J. Toufaily and M. Hmadeh, *ACS Appl. Nano Mater.*, 2024, **7**, 10003–10015.
53 J. J. Morgan, M. A. Schlautman and H. Bilinski, *Environ. Sci. Technol.*, 2021, **55**, 14426–14435.
54 M. Wekesa, M. J. Uddin and H. F. Sobh, *Int. J. Chem. Res.*, 2011, **2**, 34–37.
55 J. D. Hem, Chemical equilibria and rates of manganese oxidation, Report 1667A, 1963.
56 H. Nishihara, T. Simura, S. Kobayashi, K. Nomura, R. Berenguer, M. Ito, M. Uchimura, H. Iden, K. Arihara, A. Ohma, Y. Hayasaka and T. Kyotani, *Adv. Funct. Mater.*, 2016, **26**, 6418–6427.
57 K. Nomura, H. Nishihara, N. Kobayashi, T. Asada and T. Kyotani, *Energy Environ. Sci.*, 2019, **12**, 1542–1549.
58 L. Åkerlund, R. Emanuelsson, S. Renault, H. Huang, D. Brandell, M. Strømme and M. Sjödin, *Adv. Energy Mater.*, 2017, **7**, 1700259.
59 L. Zhong, Z. Fang, C. Shu, C. Mo, X. Chen and D. Yu, *Angew. Chem., Int. Ed.*, 2021, **60**, 10164–10171.
60 Z. Tie, Y. Zhang, J. Zhu, S. Bi and Z. Niu, *J. Am. Chem. Soc.*, 2022, **144**, 10301–10308.
61 K. Oka, S. Furukawa, S. Murao, T. Oka, H. Nishide and K. Oyaizu, *Chem. Commun.*, 2020, **56**, 4055–4058.
62 Z. Yang, L. Tong, D. P. Tabor, E. S. Beh, M.-A. Goulet, D. De Porcellinis, A. Aspuru-Guzik, R. G. Gordon and M. J. Aziz, *Adv. Energy Mater.*, 2018, **8**, 1702056.
63 D.-W. Lim and H. Kitagawa, *Chem. Soc. Rev.*, 2021, **50**, 6349–6368.
64 S. D. Talian, S. Brutti, M. A. Navarra, J. Moškon and M. Gaberscek, *Energy Storage Mater.*, 2024, **69**, 103413.
65 X. Meng, H.-N. Wang, S.-Y. Song and H.-J. Zhang, *Chem. Soc. Rev.*, 2017, **46**, 464–480.
66 Y. Cao, X. Chen, X. Li and B. Wang, *ACS Appl. Nano Mater.*, 2021, **4**, 5486–5495.
67 D. Bůžek, J. Demel and K. Lang, *Inorg. Chem.*, 2018, **57**, 14290–14297.
68 D. Bůžek, S. Adamec, K. Lang and J. Demel, *Inorg. Chem. Front.*, 2021, **8**, 720–734.
69 E.-S. M. El-Sayed, Y. D. Yuan, D. Zhao and D. Yuan, *Acc. Chem. Res.*, 2022, **55**, 1546–1560.
70 E. Laviron, *J. Electroanal. Chem. Interf. Electrochem.*, 1979, **101**, 19–28.
71 A. Molina, N. Patil, E. Ventosa, M. Liras, J. Palma and R. Marcilla, *Adv. Funct. Mater.*, 2020, **30**, 1908074.
72 D. Alván, R. Grieco, N. Patil, A. Mavrandonakis, M. Liras and R. Marcilla, *Batteries Supercaps*, 2023, **6**, e202300023.
73 G. G. Njema, R. B. O. Ouma and J. K. Kibet, *J. Renew. Energy*, 2024, **2024**, 2329261.
74 A. A. Kebede, T. Kalogiannis, J. Van Mierlo and M. Berecibar, *Renew. Sustain. Energy Rev.*, 2022, **159**, 112213.
75 S. Zhou, T. Liu, M. Strømme and C. Xu, *Angew. Chem., Int. Ed.*, 2024, **63**, e202318387.